On Secondary and Tertiary Instability in Electromagnetic Plasma Microturbulence

M.J. Pueschel[1], T. Görler[2], F. Jenko[2], D.R. Hatch[3], and A.J. Cianciara[1]

[1] *University of Wisconsin-Madison, Madison, Wisconsin 53706, USA*

[2] *Max-Planck-Institut für Plasmaphysik,*

EURATOM Association, D-85748 Garching, Germany

[3] *Institute for Fusion Studies, University of Texas at Austin, Austin, Texas 78712, USA*

Abstract

Zonal flows, widely accepted to be the secondary instability process leading to the nonlinear saturation of ion temperafture gradient modes, are shown to grow at higher rates relative to the linear mode amplitude as the plasma pressure β is increased—thus confirming that zonal flows become increasingly important in the turbulent dynamics at higher β. At the next level of nonlinear excitation, radial corrugations of the distribution function (zonal flow, zonal density, and zonal temperature) are demonstrated to modify linear growth rates moderately through perturbed-field, self-consistent gradients: on smaller scales, growth rates are reduced below the linear rate. In particular, excitation of kinetic ballooning modes well below their usual threshold is not to be expected under normal conditions. These findings strengthen the theory of the non-zonal transition [M.J. Pueschel *et al.*, Phys. Rev. Lett. **110**, 155005 (2013)].

I. INTRODUCTION

Magnetic confinement fusion devices require large pressures if practical and scientific goals like high reaction rates or continuous operation (via a large bootstrap fraction) are to be achieved. Associated with large values of the (normalized) plasma pressure are magnetic fluctuations, which are excited self-consistently by linear instabilities and the corresponding turbulence. It is thus intuitive that thorough theoretical understanding of the physics connected with magnetic fluctuations be a focus of attention.

In the context of gyrokinetic simulations, the normalized electron plasma pressure β and related effects have been the subject of various avenues of study in recent years: codes agree on electromagnetic transport values [1–5], nonlinear stabilization of ion-temperature-gradient-driven (ITG) turbulence has been found to be related to an enhancement [6] of the usual nonlinear upshift of the critical gradient [7], and advances have been made regarding microtearing turbulence [8, 9] as well as nonlinearly excited subdominant microtearing (SMT) [10, 11]. In addition to radially local gyrokinetic simulations – on which the aforementioned studies are based – strides have been made in operating gyrokinetic codes with global profiles electromagnetically [12–16]. There are, however, still many unanswered questions that can be addressed within the local limit, two of which the present paper focuses on.

Firstly, zonal flow physics [17] (where the term zonal flow refers to the electrostatic potential at both toroidal and poloidal mode number zero), which have been studied in great detail electrostatically [1, 18–23], can see important modifications in their behavior at finite values of β [24–26]. Physically, Maxwell and Reynolds stress are competing, and the shearing rate is diminished as β is increased. To understand the zonal flow dynamics quantitatively, however, both their drive and their depletion mechanisms have to be considered. The latter, in the form of nonlinear mode interaction [27–29] or the action of magnetic perturbations on the residual flow [5, 30, 31], is counteracted by the former: the energy transfer from the linear mode to the zonal mode via sidebands—a process often referred to as secondary instability, as zonal flows saturate the linear mode at the onset of turbulence. The growth rate of the secondary instability gives valuable insights into the zonal flow picture, and its dependence on β is one of the primary subjects of this paper.

Once the zonal mode has reached a sufficiently large amplitude, its components – the

$k_y = 0$ mode of the density n, the ion (electron) temperature $T_{\mathrm{i(e)}}$, or the electrostatic potential Φ – can in turn excite new or influence existing linear modes. Here, k_y is the binormal wavenumber, normalized to the inverse ion sound gyroradius ρ_{s}^{-1}. This latter process becomes possible since the zonal mode aligns with the background (equilibrium) quantities, thus effectively modifying the density gradient $\omega_n \to \omega_n + \tilde{\omega}_n$ or the ion (electron) temperature gradient $\omega_{T\mathrm{i(e)}} \to \omega_{T\mathrm{i(e)}} + \tilde{\omega}_{T\mathrm{i(e)}}$, and introducing $E \times B$ shear flow layers. The convention used throughout this paper is to use the term *tertiary instability* for linear growth based on profiles altered by the perturbations of the distribution function as measured in fully turbulent simulations. Another term – technically more accurate but rather cumbersome – for this process would be *tertiary modification of linear instability*.

Considering the potential impact of both tertiary and secondary instability on the physics of the non-zonal transition (NZT) [5, 30], particular focus is put on the behavior near the NZT threshold $\beta_{\mathrm{crit}}^{\mathrm{NZT}}$. First described in Ref. [30], the NZT can cause the heat fluxes in ITG turbulence to grow to extremely large values as a consequence of the depleting action of magnetic fluctuations on zonal flows. In that reference, it was mentioned that secondary and tertiary instability effects were found not to contribute to the transition, a statement that was based on the studies detailed in the present paper.

While all relevant information on this subject can be found in Refs. [5, 30], a brief overview of the NZT physics is given here for convenience. At sufficiently large amplitudes of the magnetic fluctuation level – and, by extension, at sufficiently large β – field lines start to decorrelate from the magnetic potential, bringing about a sudden increase in field line diffusivity. As radial diffusive electron motion depletes zonal flows at a rate proportional to β, the latter are unable, above a certain threshold, to balance the linear ITG drive and saturate the turbulence. Therefore, after some transient saturation, the linear mode starts to grow again, ultimately reaching very large heat fluxes (if the driving gradients are held constant, as is the case in radially local simulations). Note that this potentially catastrophic effect of β on the zonal flow is not in contradiction with nonlinear (or linear) β stabilization as described in Refs. [3, 6].

In the following, a brief overview of the numerical tools and parameter settings used in this work is given. Then, after a brief interlude to illustrate that mere linear physics does not provide any explanation for the NZT, secondary instability and the physics of zonal flow drive are discussed in Sec. III. Tertiary effects are detailed in Sec. IV, where previous work

is reproduced and extended to reflect the turbulent situation at the NZT threshold more accurately. Last, the results are summarized.

II. NUMERICAL FRAMEWORK

In gyrokinetic theory [32], the time scale of particle gyration about magnetic field lines is ordered out, retaining all relevant physics of low-frequency, low-collisionality plasmas. This mathematical transformation reduces the Vlasov and Maxwell equations by one dimension through elimination of the quickly oscillating gyrophase, in the process significantly improving computational efficiency.

For the numerical evaluation of the gyrokinetic equations, the GENE code [33, 34] was used in its flux tube mode of operation. Results obtained from GENE have been shown to agree well with those from other gyrokinetic codes [35–38]; in particular, for the parameters used here, the turbulent transport levels – and, by extension, the quantitative description of effects such as secondary and tertiary instability – agree well with data from other codes. See Ref. [5] for a nonlinear code-code comparison at finite-β Cyclone Base Case (CBC) [7] parameters, on which the present work is based. These parameters are: safety factor $q_0 = 1.4$, magnetic shear $\hat{s} = 0.79$, inverse aspect ratio $\epsilon_\mathrm{t} = 0.18$ of the flux surface under investigation, density gradient $\omega_n = 2.2$, and temperature gradient $\omega_T = 6.9$ (for both ions and electrons), with both gradients defined as the major radius R_0 divided by the respective gradient scale length. Both ions and electrons (at hydrogen mass ratio) have equal background temperatures. Note that *finite-β* and *electromagnetic* can be used interchangeably, as β directly regulates the magnetic fluctuation strength.

Numerical convergence was ensured; for the secondary instability investigation, resolutions were used as described in Ref. [5] unless mentioned differently in Sec. III, whereas the (linear) runs performed to ascertain tertiary effects required resolutions identical to those for linear simulations in Ref. [3]. It should be pointed out, however, that the conclusions, in particular those regarding the NZT, are valid even at somewhat reduced resolutions.

In Sec. IV, code-code comparisons were performed with a slightly modified version of the $\hat{s}$-α equilibrium model [39], whereas all other studies employed the usual GENE implemen-

tation. More specifically, the latter involves curvature-related expressions of the form

$$K_{(x|y)} \propto \frac{1}{B_0} \left(\partial_{(y|x)} B_0 + \frac{g^{x(x|y)} g^{yz} - g^{y(x|y)} g^{xz}}{g^{xx} g^{yy} - g^{yx} g^{xy}} \partial_z B_0 \right) , \tag{1}$$

in the Vlasov equation, whereas in the other version, the factor $1/B_0 \propto 1 - \epsilon_{\mathrm{t}} \cos z \sim 1$ is dropped (there exists no single standard regarding the treatment of $\mathcal{O}(\epsilon_{\mathrm{t}})$ terms)—it is to be stressed in this context that the role of the $\hat{s}$-α equilibrium has historically been that of a convenient benchmark point rather than the most accurate numerical implementation of a particular physical magnetic geometry. In the above expressions, B_0 is the background magnetic field magnitude (which varies along z, the coordinate parallel to the background field), x and y denote the radial and binormal coordinate, respectively, and g is the metric. The modified version – which corresponds to the one described in Ref. [21] – yields small quantitative changes and improves code-code agreement, but all physics-related conclusions can be expected to be valid in either framework.

The reader's attention is now focused on the description of physical results from a study of the secondary instability situation at finite β.

III. SECONDARY INSTABILITY ANALYSIS

The excitation of zonal flows by the linear ITG mode is a well-known process though which the linear mode can saturate (see Ref. [17] and references therein). It is intuitive to ask what impact β has on this secondary instability mechanism; however, to reiterate, the zonal flow drive alone does not adequately describe the zonal flow dynamics, which are also influenced by other processes.

After a brief summary on why linear effects are ruled out in explaining the NZT, the standard setup for zonal flow studies is extended to include multi-k_x modes and sidebands, which – while more complex to interpret quantitatively, mirrors the NZT-relevant scenario more closely.

In the context of the NZT, linear simulations just below and above $\beta \sim \beta_{\mathrm{crit}}^{\mathrm{NZT}}$ yield very smoothly and continuously varying growth rates, frequencies, and linear mode structures. This holds true for both the unstable modes (of ITG and trapped-electron-mode (TEM) type for CBC parameters), as well as the stable mode spectrum. Fig. 1 shows the mode spectrum (6144 linear modes were treated in this analysis). Neither does the complex frequency of
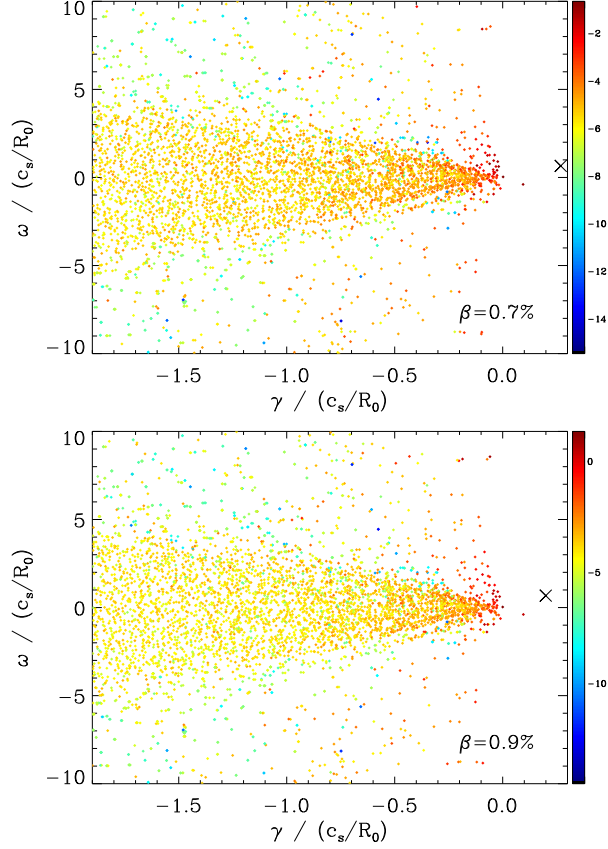
FIG. 1. (Color online) Linear mode spectrum at $k_y = 0.2$ for $\beta = 0.7\%$ (upper) and 0.9% (lower). While the most unstable (ITG) mode is marked by a black cross, the other colors logarithmically indicate the magnitude of the ion electrostatic heat flux contribution of a given mode to the turbulence (see the text). No significant qualitative changes with respect to linear eigenvalues or relative nonlinear excitation are observed as $\beta_{\mathrm{crit}}^{\mathrm{NZT}}$ is crossed.

the stable modes change much near $\beta_{\mathrm{crit}}^{\mathrm{NZT}}$ (the only clearly visible difference appears to be the somewhat shifted dominant ITG mode), nor are there important qualitative differences with respect to the relative nonlinear excitation of modes and the resulting heat fluxes—in the figure, $\log |Q_{\mathrm{i}}^{\mathrm{es}}|$ is plotted, with the colors covering the range of linear eigenmodes 2 to 6144 (some modes lie outside the plot window). Here, $Q_{\mathrm{i}}^{\mathrm{es}}$ is the ion electrostatic heat flux associated with a given linear eigenmode; it is obtained by projecting the nonlinear fluctuations onto a subset of orthogonalized linear eigenmodes (a similar analysis, along with more details on the nonlinear excitation of linear modes, can be found in Ref. [40]). For $\beta = 0.9\%$, these fluxes were measured not during the initial transient saturation stage

but at very large heat fluxes, explaining the difference in the absolute values. The most unstable mode in either plot, in both cases of ITG type, is marked by a black cross; the logarithmic amplitudes of these modes are 1.31 (for $\beta = 0.7\%$) and 1.79 (for $\beta = 0.9\%$). More details on the energetics near $\beta_{\text{crit}}^{\text{NZT}}$ can be found in Ref. [5].

As the linear physics do not exhibit any discontinuities or other modifications in their behavior near $\beta_{\text{crit}}^{\text{NZT}}$, the focus is shifted to whether the zonal flow drive (which is facilitated through the Vlasov nonlinearity) experiences any sudden changes at this point.

Many studies exist [41–45] that focus on the growth of secondary instabilities (in the case of ITG as the primary mode: zonal flows) as the saturation mechanism for a particular type of turbulence. Typically, a linear ITG mode streamer ($k_x = 0$ and $k_y \neq 0$) is held constant in time, while the zonal flow (at $k_y = 0$) grows exponentially through three-wave coupling with a sideband. More specifically, the associated growth rate γ_{ZF} depends on the amplitude of the frozen streamer, and one can define zonal flow growth (with the zonal flow electrostatic potential Φ_{ZF}) via the relation

$$\Phi_{\text{ZF}}(t) = \Phi_{\text{ZF}}(t_0)e^{\gamma_{\text{ZF}}(t-t_0)} \equiv \Phi_{\text{ZF}}(t_0)e^{\hat{\gamma}_{\text{ZF}}\Phi_{\text{ITG}}(t-t_0)} \; , \tag{2}$$

where t_0 is the point in time when the linear ITG mode is frozen and the nonlinearity is turned on. $\hat{\gamma}_{\text{ZF}}$ is independent of the linear mode's amplitude Φ_{ITG} (at $k_x = 0$). In the present paper, time units of R_0/c_s are used for normalization, and Φ is normalized to $T_{\text{e}}\rho_{\text{s}}/(eR_0)$, with the ion sound speed c_s, the electron background temperature T_{e}, and the elementary charge e.

The standard procedure for numerical studies – i.e., confining the linear mode to $k_x = 0$ – is insufficient for the present purpose: while perfectly suitable to scenarios without background magnetic shear (and thus no parallel coupling to higher k_x), for the present, more complex case, this restriction alters (or rather, under-resolves) the linear physics to an extent where NZT-relevant effects may be pushed into the linear TEM regime which appears at β values only slightly above the NZT threshold. Consequently, a somewhat different approach is indicated, where the linear mode includes a number of radially connected modes in order to resolve the linear physics more accurately. To this end, simulations are performed with a total of 17 complex modes in k_x, centered around $k_x = 0$, at $k_y = 0.3$ which corresponds to the strongest linear growth. $|k_{x,\text{min}}|$ is chosen to be 0.74, whereas the first k_x mode connected
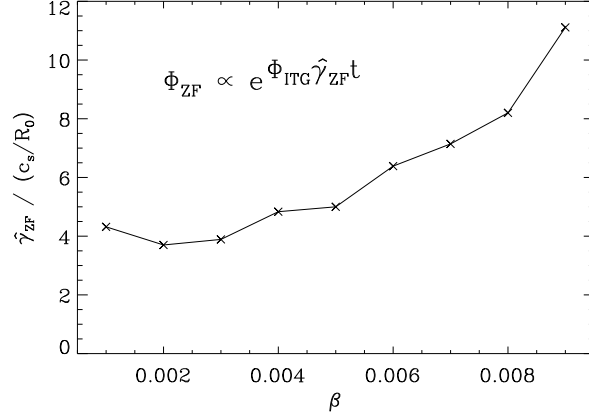
FIG. 2. Zonal flow growth as a function of β; here, the growth rate is renormalized in order to be independent of the linear mode amplitude (at $k_{x,y} = (0, 0.3)$). As β is increased, $\hat{\gamma}_{ZF}$ grows continuously, in line with the observation in Refs. [3, 6] that due to zonal flow activity, nonlinear transport is stabilized more efficiently by finite-β suppression than is the linear growth rate (not shown here). In addition, no deterioration of zonal flow excitation is observed at $\beta = 0.9\%$ just above the NZT threshold.

to $k_x = 0$ through the parallel boundary condition,

$$a(i, j, +\pi) = (-1)^{j\mathcal{N}} a(i + j\mathcal{N}, j, -\pi) \tag{3}$$

(here, a is some quantity like a potential or distribution function, i and j are the k_x and k_y mode numbers, and $\mathcal{N}$ is an integer multiplier determining the size of the radial box), is $k_x = 1.48$—like k_y, the radial wavenumber is normalized to ρ_s^{-1}. In other words, only every second radial mode is part of the extended structure of the linear ITG mode. With this setup, one effectively models two extended modes, the linear mode and a sideband, each of which consist of multiple connected k_x. In addition to the aforementioned advantage of this approach, the zonal-flow-related energetics now also mirror those of the fully turbulent system more closely both in terms of their physical nature and nonlinear simulation properties. Note, however, that like the standard approach, this concept constitutes a simplified model which clearly does not contain all mode couplings present in the full turbulence.

Now, after the ITG mode has converged in a linear simulation, not only $k_x = 0$ is frozen, but so are all modes parallelly connected to it (at $k_y = 0.3$); while all modes at $k_y = 0$ as well as the modes not connected to $k_x = 0$ at $k_y = 0.3$ are left free to evolve in time. As this pertains to the distribution function, Φ and the magnetic potential $A_parallel$ (for finite β)

8

are both treated in this fashion.

The resulting zonal flow growth rates are shown in Fig. 2 as a function of β—note that $\Phi_{\mathrm{ITG}} = |\Phi(k_x = 0, k_y = 0.3)|$ is the linear streamer amplitude; alternatively, one could use the k_x-averaged Φ of the linear mode, but both methods result in qualitatively equivalent $\hat{\gamma}_{\mathrm{ZF}}$ curves. The points in this plot were obtained by fitting linear slopes to the logarithmic zonal flow data at $k_x = k_{x,\mathrm{min}}$; similar results are obtained for higher k_x (among those values not connected to $k_x = 0$ for the linear mode). From the figure, it is straightforward to see that no sudden changes occur near $\beta_{\mathrm{crit}}^{\mathrm{NZT}}$, and that as this value is approached, the zonal flows actually grow more strongly, contrary to what one would expect if modifications to the zonal flow growth rate were responsible for the NZT. Note, however, that the absolute values shown in Fig. 2, along with the definition in Eq. (2), do not allow for a straightforward direct comparison with a linear growth rate, and are only meant to illustrate the relative change of the secondary growth rate with β.

The behavior of the zonal flows in Fig. 2 is consistent with the findings of Refs. [3, 6], where zonal flows are found to increase in strength relative to the linear γ as β is increased. More specifically, in these papers, the shearing rate $\omega_s = \langle k_x^2 \Phi_{\mathrm{fs}} \rangle$ – a standard measure of the zonal flow strength – is shown to vary continuously and rather slowly near $\beta_{\mathrm{crit}}^{\mathrm{NZT}}$. Here, the index fs denotes a flux surface average, and $\langle \ldots \rangle$ symbolizes averaging over the spatial simulation domain. Moreover, it is possible that the enhanced Dimits shift observed at higher β in Ref. [6], as well as the improved ion energy confinement reported in Ref. [46], may, at least in part, be related to this $\hat{\gamma}_{\mathrm{ZF}}$ effect—a more detailed investigation will be necessary to elucidate the exact causes.

Instead using the standard approach of describing a linear mode and its sideband at one k_x each will result in $\hat{\gamma}_{\mathrm{ZF}}$ decreasing with β (and linear mode regimes shifting with respect to the fully resolved case), in part since the parallel mode structure changes shape as β is varied (see Fig. 3 for a measure of how finite-k_x contributions become more important with larger β), an effect not properly resolved with this method. However, even there, no significant change (qualitative or quantitative) of $\hat{\gamma}_{\mathrm{ZF}}$ is observed as the NZT threshold is crossed. The qualitatively different behavior observed in this simple approach can, at least partially, be explained as follows. A relative increase of $\hat{\gamma}_{\mathrm{ZF}}$ with β – as found in Fig. 2 – is consistent with the fact that zonal flows grow faster at higher k_x: As the extended ballooning structure of the ITG mode broadens with β, its amplitude slowly and continuously moves to higher
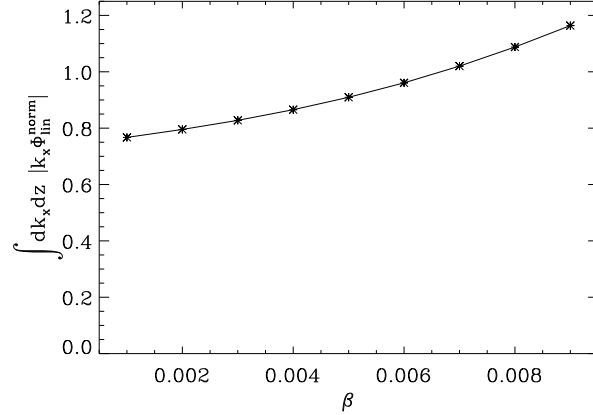
FIG. 3. Plotted here is the k_x-weighted integrated linear mode structure as function of β. Here, $\Phi_{\text{lin}}^{\text{norm}}$ indicates the linear mode centered about $k_x = 0$ with all its radial connections. This function is normalized such that its total, unweighted ballooning structure integrates to 1. It is then weighted by the radial wavenumber (a measure for the sideband growth) and integrated over k_x and z, corresponding to an integral over the ballooning angle. The resulting value increases with β, indicating that mode structure broadening is at least partially responsible for the shortcomings of the simple model which considers a linear mode only at $k_x = 0$.

k_x, in the process shifting sideband activity and coupling to the zonal modes to higher k_x. Therefore, the effective growth rate of the coupled zonal system is enhanced.

It can thus be concluded that changes in the drive of the zonal flows, which is not to be confused with the impact of the zonal flows on the turbulence, are of minimal consequence in the context of the NZT. With these findings in mind, the attention is now shifted to the next level of nonlinear excitation, tertiary instability.

IV. TERTIARY INSTABILITY AND PROFILE CORRUGATIONS

It has been demonstrated that zonal-type modes at $k_y = 0$ can, in turn, excite finite-k_y modes [42], a process also referred to as tertiary instability. The tertiary modes found here indeed bear similarities with those in Ref. [42] while also exhibiting important differences; among the latter are different responses to changes in the phase between pressure and electrostatic potential corrugations, as well as different assumptions with regard to the strength of the flow shear. A study of the precise relation of these modes will have to be

undertaken as a separate effort, however.

In this section, previous results are first reproduced before demonstrating that the conclusions drawn from them are no longer applicable to the NZT threshold once more relevant input data and more encompassing analysis techniques are used. Specifically, the amplitude of profile corrugations, their radial scale, the impact of the zonal flow, and effects from the full distribution corrugations are brought into the picture consecutively.

In the context of high-β simulations and the NZT, it has been proposed that KBMs may thus be destabilized nonlinearly [47] at a subcritical $\beta = \kappa \beta_{\mathrm{crit}}^{\mathrm{KBM}}$, where κ may be significantly smaller than one; specifically, to explain the NZT threshold, one would require $\kappa \approx 2/3$ for CBC parameters. Such scenarios rely on so-called profile corrugations [48], where local radial gradients in the self-consistent, turbulent perturbations of the density n and the temperature T can be thought of as enhancements of the corresponding background gradients ω_n and ω_T. Conversely, a local gradient of the electrostatic potential Φ implies a modification of the $E \times B$ shear and can thus exert a stabilizing influence. A quantitative analysis will have to include the correct values of the self-consistent gradients in all these quantities (at the correct length scales), as will be demonstrated below. Note that while the background density n_0 and temperature T_0 are much larger than the perturbations, the radial gradients can be of similar order, keeping in mind that $(n, T) \sim (n_0, T_0) \rho_{\mathrm{s}}/R_0$ (here, j indicates particle species):

$$\tilde{\omega}_{nj} = -\frac{R_0}{n_0} \frac{\partial n_j}{\partial x} \sim \omega_n \; , \tag{4}$$

$$\tilde{\omega}_{Tj} = -\frac{R_0}{T_{j0}} \frac{\partial T_j}{\partial x} \sim \omega_{Tj} \; . \tag{5}$$

These values are measured in the turbulent phase of a nonlinear simulation (averaging over the parallel coordinate and over time), and then the external gradients ω_n^{ext} and ω_T^{ext}, as well as the external Φ^{ext}, are turned on at those measured values for linear simulations. The former two are applied at a single wavenumber $k_x^{\mathrm{ext}}|_p$, the latter on $k_x^{\mathrm{ext}}|_\Phi$, which, in general, will be set to a different value. It is important to note that Φ^{ext} is assumed to be sufficiently weak with respect to the unperturbed equilibrium so as not to exert any influence on the background Maxwellian F_0.

To ensure that compatible approaches are used, some of the results of Ref. [47] are reproduced here. Fig. 4 shows linear growth rates both from GENE and GYRO simulations in $\hat{s}$-α geometry, where the latter were taken from the aforementioned paper—good agreement
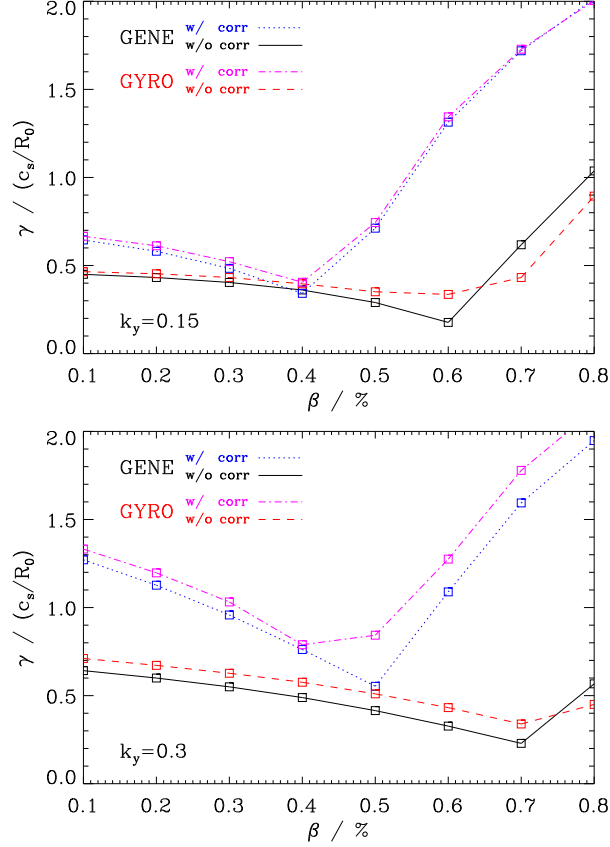
FIG. 4. (Color online) Linear growth rates as a function of β in the absence (GENE: black solid lines; GYRO: red dashed lines) and presence (GENE: blue dotted lines; GYRO: pink dash-dotted lines) of profile corrugations. The upper plot shows data for $k_y = 0.15$, the lower for $k_y = 0.3$. GYRO data points were taken from Ref. [47] (and Ref. [21] for $k_y = 0.3$ without corrugations). The profile-enhanced curves show good code-code agreement, with only small differences in the TEM regimes (which occur only when no corrugations are included) at $\beta \gtrsim 0.5\%$; this has no significant impact on $\beta_{\text{crit}}^{\text{KBM}}$, however.

is observed between both codes. This is important in particular as the GENE runs shown here use only a single $k_x^{\text{ext}}|_p$, whereas Ref. [47] utilized a more flexible approach that allows for some deformation of the sine wave profiles. Clearly, the effect of these deformations is small. It needs to be stressed, however, that the simulations in this figure do not include corrugations of Φ, and that their gradient enhancements are significantly exaggerated with respect to those typically observed in nonlinear simulations. Regardless of these objections, Ref. [47] and Fig. 4 demonstrate that in principle – i.e., if certain criteria are met – it may
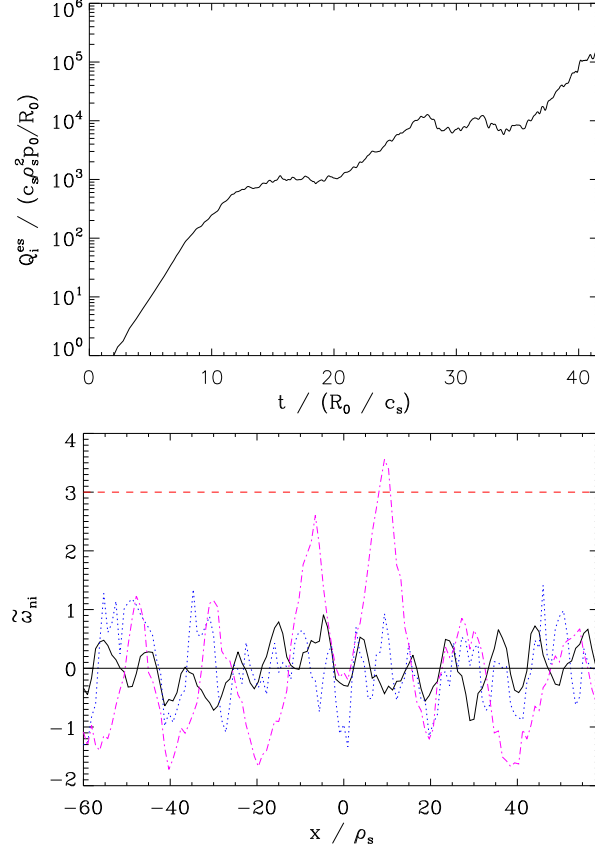
FIG. 5. Upper plot: ion electrostatic heat flux for the parameters used to obtain the corrugations in Ref. [47]. There are at least two transient saturation regimes, one at $Q_i^{es} \sim 10^3$ and one at $Q_i^{es} \sim 10^4$, the latter well inside the NZT. Both phases exhibit different properties in terms of their corrugation amplitudes and $k_x^{ext}|_p$: in the lower plot, the ion density corrugations are shown for the first (blue dotted line) and second regime (pink dash-dotted line). The former is much more similar to the corrugations at slightly lower $\beta = 0.2\%$ (black solid line). The background gradient is shown as a dashed red line for comparison.

be possible to excite modes subcritically, in particular KBMs. Whether this scenario is applicable to any present-day or future fusion experiments is still an unanswered question, but the following analyses suggest that it may be difficult to observe subcritical excitation in realistic cases.

Ref. [47] shows measured radial corrugations of $\tilde{\omega}_{n,T} \lesssim 0.8\omega_{n,T}$ (or $X \lesssim 1.8$ in their notation) for their standard case at $\beta = 0.3\%$. Reproducing these values quantitatively requires the following approach: As β lies just above β_{crit}^{NZT}, to obtain agreement, corrugations

had to be measured in the transient saturated phase around $t \sim 30$, see Fig. 5 (upper plot). This, however, represents a second transient saturated phase—the first one can be found around $t \sim 15$. Note that only the fluxes during the first phase are consistent with those at slightly lower β, meaning the second phase is already part of the NZT process. If profile corrugations and subcritical mode excitation are to be investigated in the context of the NZT, it is more appropriate to measure corrugations either in the first phase at $t \sim 15$ – as hypothetical NZT-causing, subcritical KBMs would have to be excited there in order for the heat fluxes to ever reach the second, high-flux phase at $t \sim 30$ – or in simulations just below $\beta_{\text{crit}}^{\text{NZT}}$, which will have much better statistics. As illustrated in Fig. 5 (lower plot), both methods lead to both significantly lower $\tilde{\omega}_{n,T}$ – with $\tilde{\omega}_{n,T} \lesssim 0.3\omega_{n,T}$ at $\beta = 0.2\%$ – and a $k_x^{\text{ext}}|_p$ of twice that used to produce the curves shown in Fig. 4. The impact of these differences will become apparent in the study presented below.

The above results pertain to the GA-std parameter case; for other parameters, the picture is not complicated by multiple transient saturation regimes: Turning again to the CBC and the relevance of profile corrugations to the NZT for these parameters, time-averaged corrugation data from a nonlinear simulation at $\beta = 0.7\%$ is shown in Fig. 6. Note that the temperature corrugations were obtained through $T = (T_\parallel + 2T_\perp)/2$. These plots demonstrate that the observed corrugations in n and T have mostly $k_x^{\text{ext}}|_p = 0.74$ (corresponding to radial mode number $n = 12$), with some component at $n = 4$, or $k_x^{\text{ext}}|_p = 0.25$; whereas Φ dominantly lives on the $n = 1$ mode, corresponding to $k_x^{\text{ext}}|_\Phi = 0.062$. Not shown is the significant temporal variation which may pose another difficulty for tertiary modes which thus see their corrugation drive changing continuously, and which will be commented on in more detail below.

A tertiary instability analysis based on these values can be found in Fig. 7. Simulations, regardless of $k_x^{\text{ext}}|_p$ and k_y, retain seven k_x connections on each side of $k_x = 0$, and use $N_{v\parallel} = 96$; both choices were made to resolve the linear physical properties fully—the nonlinear case (which, in particular, has fewer radial connections at higher k_y) can be expected to behave very similarly, however. The plots demonstrate that for large $\omega_{n,T}^{\text{ext}}$ (and no Φ^{ext}), subcritical destabilization of KBMs is indeed possible for CBC parameters (the original $\beta_{\text{crit}}^{\text{KBM}}$ lies near 1.3% for both k_y shown here [3]). However, the enhancement used for that curve was $\omega_{n,T}^{\text{ext}} = 1.5\omega_{n,T}$, the same relative enhancement as in Fig. 4, with $k_x^{\text{ext}}|_p = 0.25$. With the measured, lower values $\omega_n^{\text{ext}} = 0.5$ and $\omega_n^{\text{ext}} = 3$ (which can be inferred as good estimates
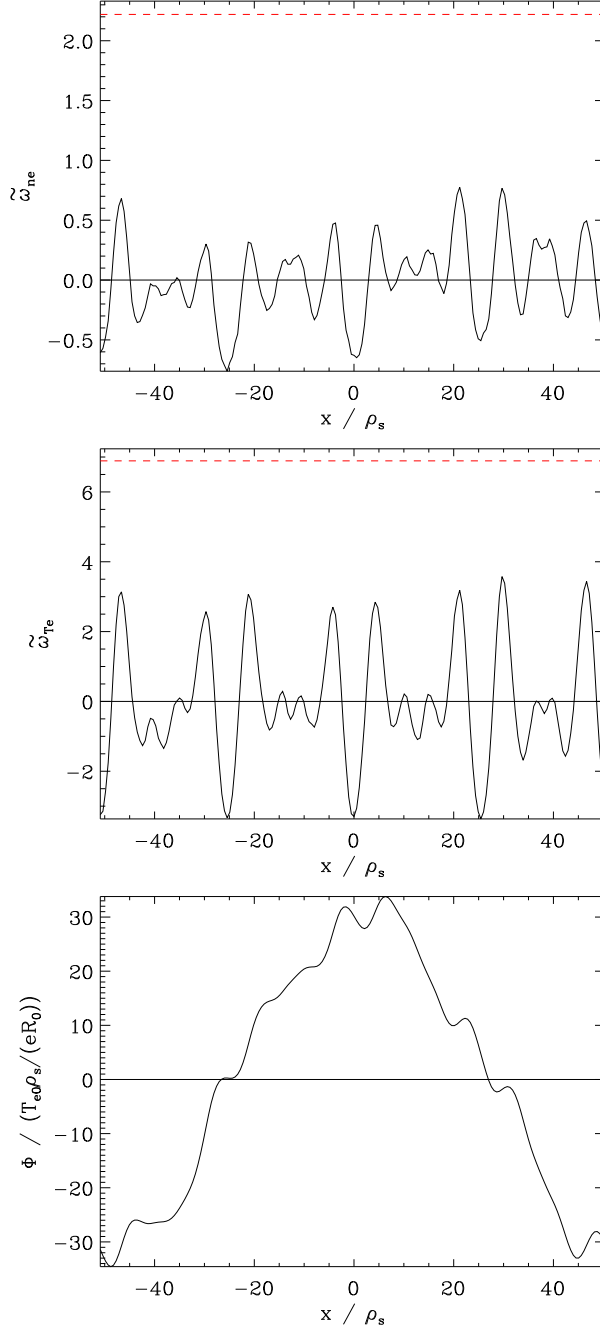
FIG. 6. (Color online) Radial profile corrugations for CBC parameters, measured at $\beta = 0.7\%$ and averaged over the saturated phase of the simulation. The quantities shown are the self-consistent density gradient $\tilde{\omega}_{ne}$ and temperature gradient $\tilde{\omega}_{Te}$ of the electrons (similar properties are found for the ions, at slightly lower values), as well as the electrostatic potential Φ. The former two exhibit spatial oscillations mostly on two scales, $L_x/12$ and $L_x/4$, whereas Φ varies on a scale of L_x due to zonal flow activity. Dashed red lines indicate the values of the relevant background gradients.
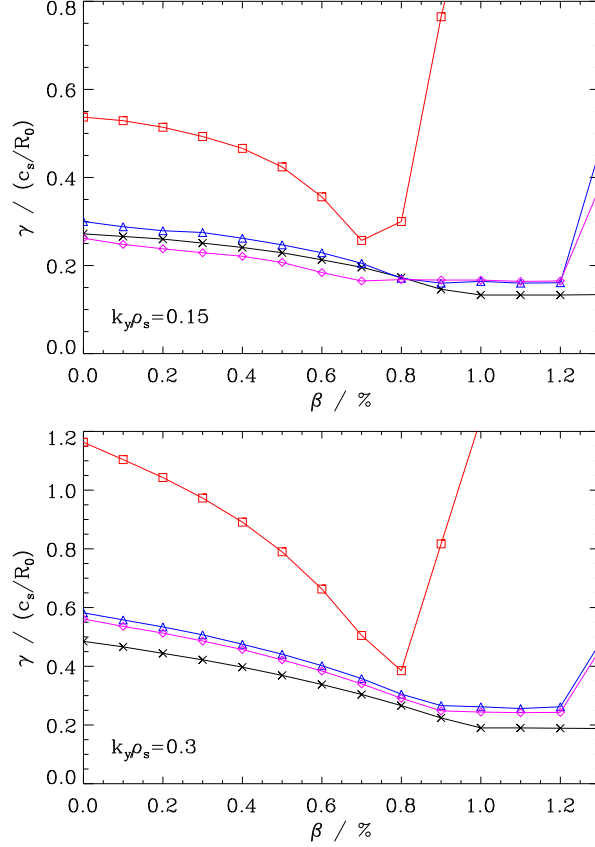
15

FIG. 7. (Color online) Growth rates in the presence of profile corrugations for CBC parameters at two different k_y. Black crosses mark the original γ without corrugations, red squares correspond to artificially large $\omega_n^{\text{ext}} = 3.33$ and $\omega_T^{\text{ext}} = 10.34$, resulting in significant destabilization. The effect is far less pronounced for realistic values (blue triangles), compare Fig. 6. Further reduction of the enhancement is observed when adding $\Phi^{\text{ext}} = 30$ (pink diamonds). Subcritical KBMs are seen only for artificially large corrugations.

from Fig. 6), the growth rate enhancement is significantly reduced, and no subcritical KBMs is visible. Adding Φ^{ext} at $k_x^{\text{ext}}|_\Phi = 0.062$ further reduces γ. Lastly, Φ corrugations were neglected again, but since the peaks in Fig. 6 have widths consistent with $k_x^{\text{ext}}|_p = 0.74$, simulations were performed with that value and the same realistic $\omega_{n,T}^{\text{ext}}$ as mentioned above. The results are not shown in the plot for the simple reason that they almost perfectly coincide with the data points obtained without any corrugations: the radial regions of enhanced gradients are too small for tertiary effects to appear.

To ascertain the role of the phases of the corrugations, simulations were performed with the phase angle ϕ varied between $\phi = (0, \pi/2, \pi, 3\pi/2)$. Here, $\phi(n)$ and $\phi(T)$ were always

set to an identical value. Both the absolute phase and, in cases with Φ^{ext}, the relative phase of $\phi(\Phi)$ had very little impact on the resulting growth rates.

Another feature of these simulations is that, not surprisingly, the ITG and TEM regimes are also affected by the corrugations. While for realistic corrugation amplitudes, these effects are relatively small, such modifications may be interesting to take into account for quasilinear models (see, e.g., Refs. [49, 50])—note, however, that for the most relevant $k_x^{\text{ext}}|_p = 0.74$, no enhancement is seen at any β. With regard to the corrugations present in the simulation of Fig. 5, it can be conjectured that the different $k_x^{\text{ext}}|_p$ in the second transient saturation phase (relative to the first) may help boost the ITG mode at that point, consistent with the picture described in Ref. [47], even when this process does not bring about the NZT in the first place.

Next, it is shown that taking into account effects due to fast temporal variation of the corrugations are unlikely to change this picture.

The time averages used in this section typically stretch over windows much longer than a correlation time. In general, it is possible that for periods (much) shorter than the whole average time, bursts of corrugation amplitudes occur, with subcritical excitation of KBMs during these events.

Thus, it is necessary to take a closer look at time-resolved corrugations, which are plotted in Fig. 8. $\tilde{\omega}_{Ti}(x, t)$ exhibits two important features: First, while the time-averaged value is generally representative of the resolved behavior, there are isolated spikes up to $\tilde{\omega}_{Ti} \lesssim \omega_{Ti}$, lasting typically a few time units. Second, the characteristic radial structure with of $L_x/12$ that was observed in the time-averaged plot is very prominent also in the resolved one. The density and electron temperature corrugations behave similarly (not shown in the figure); albeit with some extremely short but strong bursts, during which a new mode would not have enough time to grow much. $\Phi(x, t)$, however, shows markedly different features: it is far less bursty, and instead moves back and forth through the radial box—this means that the time-averaged value underestimates the instantaneous corrugation by more than a factor of two. As mentioned above, the varying phase of $\Phi(x, t)$ is not expected to have any bearing on the tertiary growth rates for the present case.

Based on these findings, one could conjecture that subcritical KBMs are excited during one of the $\tilde{\omega}_{Ti}$ bursts; while it is doubtful that the mode would be able to reach system-relevant amplitudes during that short phase, another tertiary instability analysis was carried
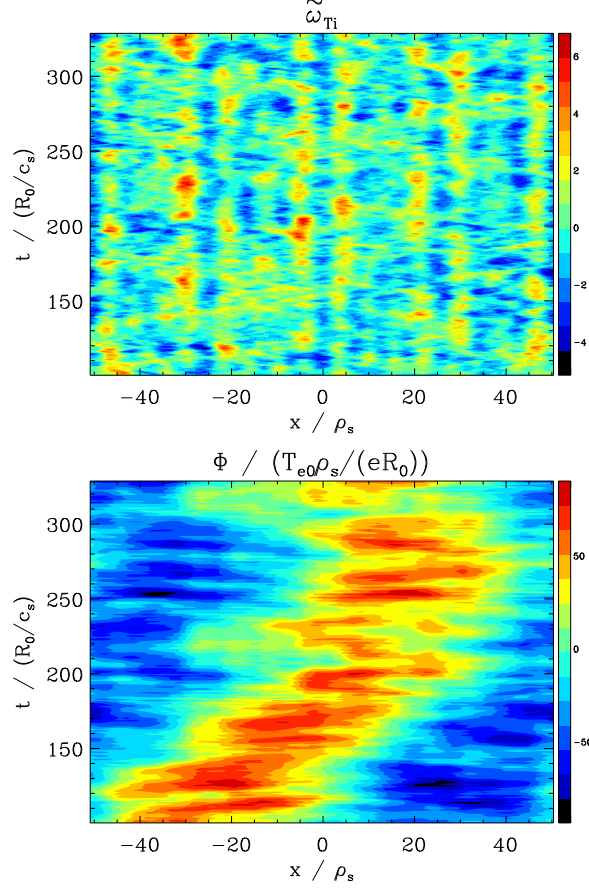
FIG. 8. (Color online) Self-consistent ion temperature gradient (upper) and Φ corrugations (lower) as functions of radial coordinate and time, at $\beta = 0.7\%$. For the former, clear vertical structures of width $L_x/12$ can been seen, with only short bursts (in particular the red regions). The latter meanders back and forth but is otherwise relatively homogeneous in its structure.

out, this time with values near the peaks of the bursts, with $\omega_{Ti,e}^{ext} = 6$, $\omega_n^{ext} = 2$, and $\Phi^{ext} = 70$, at the proper radial length scales. The results are not surprising, see Fig. 9: due to the narrow space available to the pressure corrugations, not much enhancement occurs, and instead, the larger Φ corrugations stabilize the linear mode measurably. Note that the variability in the tertiary growth rates is a result of extensive beating of competing linear modes. Even when Φ corrugations are neglected (blue diamonds in the plot), the tertiary growth rates do not deviate very significantly from the linear ones, and again the subcritical KBM fails to surface.

Time-resolved analysis of the corrugations therefore is not yielding results supportive of subcritical excitation. Next, full distribution data from nonlinear simulations is used for the
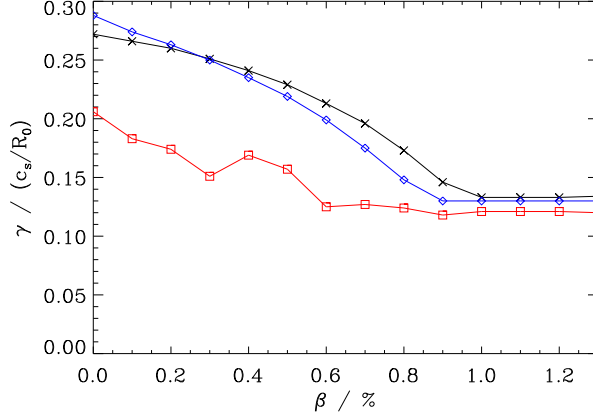
18

FIG. 9. (Color online) Tertiary growth rates at $k_y = 0.15$ with corrugations mimicking enhanced conditions during turbulent bursts (red squares), see the text, as a function of β. Black crosses denote the linear rates for comparison, whereas blue diamonds correspond to the same setup as the red squares, only without Φ corrugations. The larger Φ^{ext} easily overcomes any destabilizing effect of the pressure corrugations. In fact, the tertiary points have the ITG mode stabilized so strongly that throughout the entire β range shown here it is either subdominant or has γ values comparable with the TEM (which appears to be less affected by Φ^{ext}).

corrugations, rather than modeled corrugations in only Φ and the pressure.

Maximal realism of the analysis is retained when using corrugation data of the (perturbed) distribution function directly and studying its impact on tertiary instability. The distribution was time-averaged during the saturated phase of a separate nonlinear simulation at $\beta = 0.7\%$ (i.e., just below $\beta_{\text{crit}}^{\text{NZT}}$), with the corresponding n, T, and Φ corrugations being very similar to those in Fig. 6 quantitatively. Growth was then measured the same way as in the previous studies, but with the resolutions of the nonlinear simulation (except only one finite k_y value was included per run), implying both that higher k_y retain fewer radial connections and that sidebands are included which are not connected to $k_x = 0$.

The results of this study are shown in Fig. 10: at small k_y, the tertiary behavior closely follows that of the linear ITG mode, before the tertiary curve falls below the linear one just above $k_y = 0.15$—coincidentally, the nonlinear heat flux peaks at that k_y. The frequencies seem not to be affected by this stabilization; however, with the latter appearing to be more pronounced for the ITG mode than for the TEM, a regime change occurs where the TEM becomes the dominant tertiary instability. This, however, happens at scales where the heat
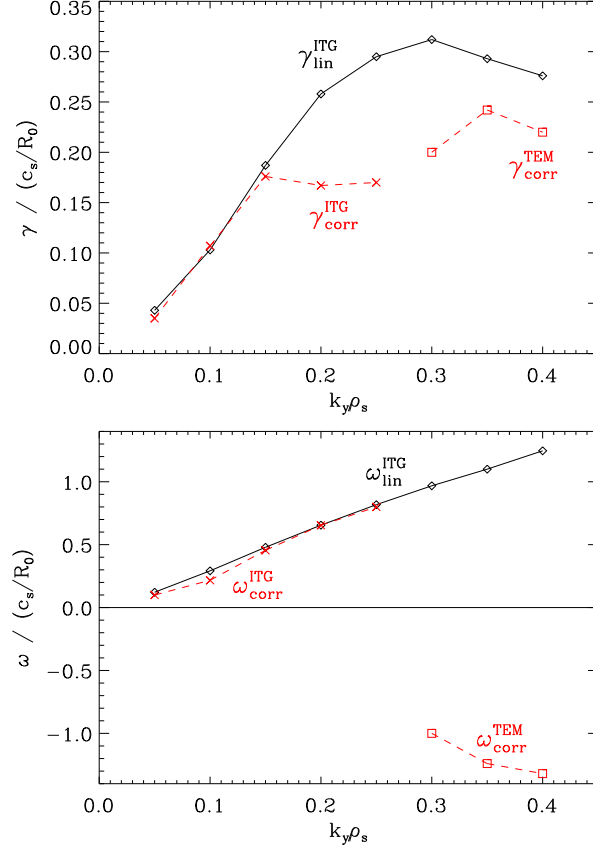
FIG. 10. (Color online) Tertiary growth rates (upper graph) and frequencies (lower graph) as functions of k_y, obtained with realistic corrugations from the distribution function (dashed red curves). Crosses indicate dominant ITG growth, squares TEM. For comparison, the linear growth rates and frequencies are plotted as black diamonds, with ITG being the dominant instability throughout the k_y range shown here. For large scales (small k_y), little modification is observed tertiarily, whereas larger scales exhibit some stabilization.

flux has already dropped to relatively small values (not shown).

Before turning to the conclusions, one more argument is presented which is based on the lack of KBM frequency signatures during the NZT: Another indication that subcritical excitation cannot be responsible for the NZT threshold can be found in the nonlinear frequencies: both during the runaway phase and during the (likely unphysical, but numerically relevant) second saturated phase at extreme heat flux levels, the frequency signatures match the linear ITG frequencies very well [30]. In contrast, the frequencies of the tertiary KBMs – which are very similar to those of the linear KBMs [3] – are much larger than typical ITG values and would be easily discernible. Note that the nonlinear frequencies reported
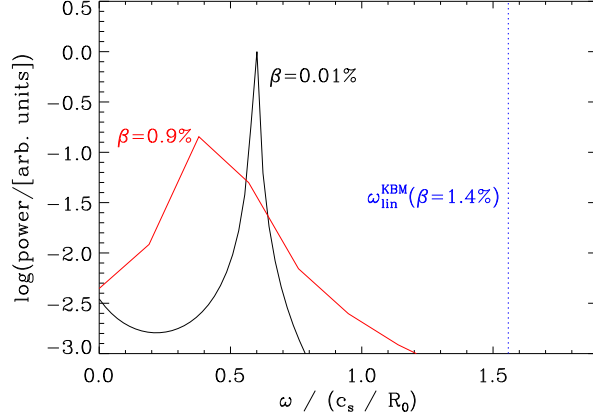
20

FIG. 11. (Color online) Logarithmic power as function of mode frequency. Black solid curve: electrostatic turbulence (CBC parameters). Red solid curve: turbulence in the high-flux saturated regime at $\beta = 0.9\%$. Neither data has significant contributions near the linear KBM frequency (blue dotted line).

in Ref. [3] for $\beta \geq 0.8\%$ (which apply to the transient saturation phase), while not exactly matching the linear ITG values, are still much lower than KBM frequencies—as opposed to linearly dominant KBMs which have strong signatures in KBM-driven turbulence [3, 6].

To further strengthen this point, the frequency analysis algorithm PMUSIC [51] was used on CBC data in order to obtain better access to subdominant frequencies. For this technique, the (z-averaged) electrostatic potential at a given k_y was analyzed according to the following prescription: A data matrix is constructed whose upper half contains the input data divided into overlapping windows—the lower half contains the transpose and complex conjugate of the same data. Using singular value decomposition on the data matrix, one then selects the less prominent singular values and designates them as noise components. Finally, one essentially takes the inverse of the filtered noise eigenvectors—whenever the noise level becomes small compared to the signal at some given frequency, this quantity becomes very large. In Ref. [52], all necessary details are readily summarized, and the reader is therefore referred to that publication (note that in the present paper, no time-dependent frequency signatures are investigated, however).

For the CBC, the resulting frequency spectrum is found in Fig. 11, in this case for $k_y = 0.1$. The nonlinear frequencies are compared for the saturated regime of a simulation in the electrostatic limit ($\beta = 0.01\%$, black curve) as a baseline and of one that has undergone

an NZT (at $\beta = 0.9\%$), meaning the frequencies are analyzed during the high-flux saturated phase (red curve). Clearly, the spectra in either case peak far away from the values one would expect if KBM activity played a significant role, and neither are any subdominant contributions visible near the KBM frequency. Note that the latter, marked with a blue dotted line, is defined as the frequency of the linear KBM just after it becomes the dominant mode at this particular k_y. These findings underscore the absence of KBM-like features in the simulations that have experienced an NZT.

Below, the findings of this paper are summarized.

V. SUMMARY

Zonal flows were studied with respect to their growth as a secondary instability excited by the primary ITG mode—the renormalized growth rate $\hat{\gamma}_{\mathrm{ZF}}$ was shown to have increased roughly three-fold at $\beta \sim 1\%$ relative to the electrostatic limit. Unlike in previous zonal flow simulations, the linear mode, the sideband, and the zonal flow were each resolved by multiple, connected k_x, leading to shifting k_x contributions when β was changed—this approach is more representative of the situation in nonlinear simulations. While not sufficient by themselves to explain the full zonal flow dynamics of ITG turbulence, these findings corroborate the theory that zonal flows play a larger role in the saturation for higher β. In addition, their drive was found not to exhibit any qualitative changes – and, in fact, grew stronger – as β crossed the NZT threshold; supporting the statements in Refs. [5, 30] that it is zonal flow decay rather than a change in zonal flow drive that brings about this transition.

Regarding tertiary instability, here defined to mean the impact of zonal mode corrugations on linear growth, multiple stages of realism were distinguished. At very large turbulent pressure gradient fluctuations $\tilde{\omega}_{nj}$ and $\tilde{\omega}_{Tj}$ on a scale of $1/(\hat{s}k_{y,\mathrm{min}})$, the system is able to enhance linear growth significantly and even excite KBMs subcritically. When using realistic values and scales for the corrugations, these effects vanish, however; and at higher k_y, moderate stabilization is observed. It is thus concluded that tertiary instability – and, in particular, subcritical excitation – does not affect the NZT threshold (this result is expected to hold universally, whereas the other findings of this paper, such as the enhanced zonal flow growth at higher β, may apply only to certain parameter regimes). This differs from the conclusions in Ref. [47] in large part because their measurement of the profile corrugations

was taken at a point during the simulations when the NZT had already elevated the turbulent amplitudes significantly—leading to the subcritical excitation of KBMs in Ref. [47] which are also shown in Fig. 4. Therefore, while subcritical KBMs may, under certain conditions, play a role in further boosting heat fluxes at later times, they are unable to bring about the NZT in the first place.

ACKNOWLEDGMENTS

[1] Y. Chen, S.E. Parker, B.I. Cohen, A.M. Dimits, W.M. Nevins, D. Shumaker, V.K. Decyk, and J.N. Leboeuf, Nucl. Fusion **43**, 1121 (2003)

[2] J. Candy, Phys. Plasmas **12**, 72307 (2005)

[3] M.J. Pueschel, M. Kammerer, and F. Jenko, Phys. Plasmas **15**, 102310 (2008)

[4] A.G. Peeters, Y. Camenen, F.J. Casson, W.A. Hornsby, A.P. Snodin, D. Strintzi, and G. Szepesi, Comp. Phys. Commun. **180**, 2650 (2009)

[5] M.J. Pueschel, D.R. Hatch, T. Görler, W.M. Nevins, F. Jenko, P.W. Terry, and D. Told, *Properties of High-β Microturbulence and the Non-Zonal Transition*, submitted to Phys. Plasmas (2013)

[6] M.J. Pueschel and F. Jenko, Phys. Plasmas **17**, 062307 (2010)

[7] A.M. Dimits, G. Bateman, M.A. Beer, B.I. Cohen, W. Dorland, G.W. Hammett, C. Kim, J.E. Kinsey, M. Kotschenreuther, A.H. Kritz, L.L. Lao, J. Mandrekas, W.M. Nevins, S.E. Parker, A.J. Redd, D.E. Shumaker, R. Sydora, and J. Weiland, Phys. Plasmas **7**, 969 (2000)

[8] H. Doerk, F. Jenko, M.J. Pueschel, and D.R. Hatch, Phys. Rev. Lett. **106**, 155003 (2011)

[9] W. Guttenfelder, J. Candy, S.M. Kaye, W.M. Nevins, E. Wang, R.E. Bell, G.W. Hammett, B.P. LeBlanc, D.R. Mikkelsen, and H. Yuh, Phys. Rev. Lett. **106**, 155004 (2011)

[10] D.R. Hatch, P.W. Terry, F. Jenko, F. Merz, M.J. Pueschel, W.M. Nevins, and E. Wang, Phys. Plasmas **18**, 055706 (2011)

[11] D.R. Hatch, M.J. Pueschel, F. Jenko, W.M. Nevins, P.W. Terry, and H. Doerk, Phys. Rev. Lett. **108**, 235002 (2012)

[12] L. Villard, A. Bottino, S. Brunner, A. Casati, J. Chowdhury, T. Dannert, R. Ganesh, X. Garbet, T. Görler, V. Grandgirard, R. Hatzky, Y. Idomura, F. Jenko, S. Jolliet, S. Khosh Aghdam, X. Lapillonne, G. Latu, B.F. McMillan, F. Merz, Y. Sarazin, T.M. Tran, and T. Vernay, Plasma Phys. Control. Fusion **52**, 124038 (2010)

[13] W. Wan, S.E. Parker, Y. Chen, Z. Yan, R.J. Groebner, and P.B. Snyder, Phys. Rev. Lett. **109**, 185004 (2012)

[14] A. Mishchenko and A. Zocco, Phys. Plasmas **19**, 122104 (2012)

[15] W. Zhang, I. Holod, Z. Lin, and Y. Xiao, Phys. Plasmas **19**, 022507 (2012)

[16] E.M. Bass and R.E. Waltz, Phys. Plasmas **20**, 012508 (2013)

[17] P.H. Diamond, S.-I. Itoh, K. Itoh, and T.S. Hahm, Plasma Phys. Control. Fusion **47**, R35 (2005)

[18] P.H. Diamond and Y.-B. Kim, Phys. Fluids B **3**, 1626 (1991)

[19] P.H. Diamond, M.N. Rosenbluth, E. Sanchez, C. Hidalgo, B. Van Milligen, T. Estrada, B. Brañas, M. Hirsch, H.J. Hartfuss, and B.A. Carreras, Phys. Rev. Lett. **84**, 4842 (2000)

[20] J. Li and Y. Kishimoto, Phys. Rev. Lett. **89**, 115002 (2002)

[21] J. Candy and R.E. Waltz, J. Comp. Phys. **186**, 545 (2003)

[22] F. Jenko, Phys. Lett. A **351**, 417 (2006)

[23] T.-H. Watanabe and H. Sugama, Nucl. Fusion **46**, 24 (2006)

[24] E. Kim, T.S. Hahm, and P.H. Diamond, Phys. Plasmas **8**, 3576 (2001)

[25] B.D. Scott, New J. Phys. **7**, 92 (2005)

[26] V. Naulin, A. Kendl, O.E. Garcia, A.H. Nielsen, and J. Juul Rasmussen, Phys. Plasmas **12**, 052515 (2005)

[27] K.D. Makwana, P.W. Terry, J.-H. Kim, and D.R. Hatch, Phys. Plasmas **18**, 012302 (2011)

[28] M. Nakata, T.-H. Watanabe, and H. Sugama, Phys. Plasmas **19**, 022303 (2012)

[29] K.D. Makwana, P.W. Terry, and J.-H. Kim, Phys. Plasmas **19**, 062310 (2012)

[30] M.J. Pueschel, P.W. Terry, F. Jenko, D.R. Hatch, W.M. Nevins, T. Görler, and D. Told, Phys. Rev. Lett. **110**, 155005 (2013)

[31] P.W. Terry, M.J. Pueschel, D. Carmody, and W.M. Nevins, in preparation (2013)

[32] A.J. Brizard and T.S. Hahm, Rev. Mod. Phys. **79**, 421 (2007)

[33] F. Jenko, W. Dorland, M. Kotschenreuther, and B.N. Rogers, Phys. Plasmas **7**, 1904 (2000)

[34] see `http://gene.rzg.mpg.de` for code details and access

[35] W.M. Nevins, J. Candy, S. Cowley, T. Dannert, A. Dimits, W. Dorland, C. Estrada-Mila, G.W. Hammett, F. Jenko, M.J. Pueschel, and D.E. Shumaker, Phys. Plasmas **13**, 122306 (2006)

[36] G.L. Falchetto, B.D. Scott, P. Angelino, A. Bottino, T. Dannert, V. Grandgirard, S. Janhunen, F. Jenko, S. Jolliet, A. Kendl, B.F. McMillan, V. Naulin, A.H. Nielsen, M. Ottaviani, A.G. Peeters, M.J. Pueschel, D. Reiser, T.T. Ribeiro, and M. Romanelli, Plasma Phys. Control. Fusion **50**, 124015 (2008)

[37] X. Lapillonne, B.F. McMillan, T. Görler, S. Brunner, T. Dannert, F. Jenko, F. Merz, and L. Villard, Phys. Plasmas **17**, 112321 (2010)

[38] M.J. Pueschel, F. Jenko, D. Told, and J. Büchner, Phys. Plasmas **18**, 112102 (2011)

[39] J. Connor, R. Hastie, and J. Taylor, Phys. Rev. Lett. **40**, 396 (1978)

[40] D.R. Hatch, M.J. Pueschel, F. Jenko, W.M. Nevins, P.W. Terry, and H. Doerk, Phys. Plasmas **20**, 012307 (2013)

[41] S.C. Cowley, R.M. Kulsrud, and R. Sudan, Phys. Fluids B **3**, 2767 (1991)

[42] B.N. Rogers, W. Dorland, and M. Kotschenreuther, Phys. Rev. Lett. **85**, 5336 (2000)

[43] F. Jenko and W. Dorland, Phys. Rev. Lett. **89**, 225001 (2002)

[44] D. Strintzi and F. Jenko, Phys. Plasmas **14**, 042305 (2007)

[45] P. Xanthopoulos, F. Merz, T. Görler, and F. Jenko, Phys. Rev. Lett. **99**, 035002 (2007)

[46] J. Citrin, C. Bourdelle, J. Garcia, J.W. Haverkort, F. Jenko, G.M.D. Hogeweij, T. Johnson, P. Mantica, M.J. Pueschel, D. Told, and JET-EFDA contributors *Nonlinear microturbulence stabilization by fast ions in tokamaks*, in preparation (2013)

[47] R.E. Waltz, Phys. Plasmas **17**, 072501 (2010)

[48] R.E. Waltz, M.E. Austin, K.H. Burrell, and J. Candy, Phys. Plasmas **13**, 052301 (2006)

[49] C. Bourdelle, X. Garbet, F. Imbeaux, A. Casati, N. Dubuit, R. Guirlet, and T. Parisot, Phys. Plasmas **14**, 112501 (2007)

[50] J. Citrin, C. Bourdelle, P. Cottier, D.F. Escande, O.D. Gurcan, D.R. Hatch, G.M.D. Hogeweij, F. Jenko, and M.J. Pueschel, Phys. Plasmas **19**, 062305 (2012)

[51] T. Iwata, Y. Goto, and H. Susaki, Meas. Sci. Technol. **12**, 2178 (2001)

[52] L. Vermare, P. Hennequin, Ö.D. Gürcan, and the Tore Supra Team, Nucl. Fusion **52**, 063008 (2012)